Biosensors and Bioelectronics 237 (2023) 115545

Contents lists available at ScienceDirect

Biosensors and Bioelectronics

journal homepage: www.elsevier.com/locate/bios

Simple, miniaturized biosensors for wireless mapping of thermoregulatory responses

Seyong Oh [a,b,1,**], Jae-Young Yoo [b,1], Woo-Youl Maeng [b,1], Seonggwang Yoo [b], Tianyu Yang [b], Susan M. Slattery [c,d], Sara Pessano [c], Emily Chang [b], Hyoyoung Jeong [e], Jihye Kim [b], Hak-Young Ahn [b], Yeongdo Kim [b], Joohee Kim [f], Shuai Xu [b,g], Debra E. Weese-Mayer [c,d], John A. Rogers [b,*]

[a] Division of Electrical Engineering, Hanyang University ERICA, Ansan, 15588, Republic of Korea
[b] Querrey Simpson Institute for Bioelectronics, Northwestern University, Evanston, IL, 60208, USA
[c] Stanley Manne Children's Research Institute, Ann & Robert H Lurie Children's Hospital of Chicago, Chicago, IL, 60611, USA
[d] Department of Pediatrics, Northwestern University Feinberg School of Medicine, Chicago, IL, 60611, USA
[e] Department of Electrical and Computer Engineering, University of California Davis, Davis, CA, 95616, USA
[f] Center for Bionics, Biomedical Research Division, Korea Institute of Science and Technology, Seoul, 02792, Republic of Korea
[g] Sibel Health, Niles, IL, 60714, USA

ARTICLE INFO

Keywords:
Bioelectronics
Wireless sensors
Thermoregulatory responses
Health monitoring

ABSTRACT

Temperature is the most commonly collected vital sign in all of clinical medicine; it plays a critical role in care decisions related to topics ranging from infection to inflammation, sleep, and fertility. Most assessments of body temperature occur at isolated anatomical locations (e.g. axilla, rectum, temporal artery, or oral cavity). Even this relatively primitive mode for monitoring can be challenging with vulnerable patient populations due to physical encumbrances and artifacts associated with the sizes, weights, shapes and mechanical properties of the sensors and, for continuous monitoring, their hard-wired interfaces to data collection units. Here, we introduce a simple, miniaturized, lightweight sensor as a wireless alternative, designed to address demanding applications such as those related to the care of neonates in high ambient humidity environments with radiant heating found in incubators in intensive care units. Such devices can be deployed onto specific anatomical locations of premature infants for homeostatic assessments. The estimated core body temperature aligns, to within 0.05 °C, with clinical grade, wired sensors, consistent with regulatory medical device requirements. Time-synchronized, multi-device operation across multiple body locations supports continuous, full-body measurements of spatio-temporal variations in temperature and additional modes of determining tissue health status in the context of sepsis detection and various environmental exposures. In addition to thermal sensing, these same devices support measurements of a range of other essential vital signs derived from thermo-mechanical coupling to the skin, for applications ranging from neonatal and infant care to sleep medicine and even pulmonary medicine.

1. Introduction

Temperature is the most commonly collected vital sign in clinical medicine (Ahrens, 2008; Cardona-Morrell et al., 2016; Elliott and Coventry, 2012; Lockwood et al., 2004). Clinical thermometers remain one of the most widely deployed medical devices globally (Amare et al., 2021; Crawford et al., 2006; Tamura et al., 2018). Measurements of body and skin temperature are essential for clinical decision-making related to infection, inflammation, sleep, fertility and others. Most assessments of temperature involve episodic measurements at specific anatomical locations (e.g. axilla, rectum, temporal artery, or oral cavity), conducted manually by clinicians or caregivers. This cumbersome process of monitoring involves additional challenges when applied to vulnerable patient populations. For example, wired probes represent the

* Corresponding author. Querrey Simpson Institute for Bioelectronics, Northwestern University, Evanston, IL, 60208, USA
** Corresponding author. Division of Electrical Engineering, Hanyang University ERICA, Ansan, 15588, Republic of Korea
E-mail addresses: seyongoh89@hanyang.ac.kr (S. Oh), jrogers@northwestern.edu (J.A. Rogers).
[1] These authors contributed equally to this work.

https://doi.org/10.1016/j.bios.2023.115545
Received 28 April 2023; Received in revised form 11 July 2023; Accepted 21 July 2023
Available online 26 July 2023
0956-5663/© 2023 Elsevier B.V. All rights reserved.

standard of care in pediatric medicine for radiant warmers and incubator units, to avoid hypothermia or overheating (Smith et al., 2013; Uslu et al., 2011). Such measurements are essential for neonates of significant prematurity, where thermal homeostasis typically requires active control and/or medical intervention (Castrodale and Rinehart, 2014; Donnellan et al., 2020; Knobel, 2014).

A growing body of scientific evidence supports the use of continuous physiological monitoring with wireless, skin-interfaced sensors to identify clinical deterioration at early stages, to prevent unplanned intensive care unit admissions, to enhance patient comfort, and to reduce hospital stays (Areia et al., 2021; Eddahchouri et al., 2022; Weenk et al., 2019; Xu et al., 2020, 2022). For temperature, several such wireless options are now commercially available (e.g. TempTraq from BlueSpark, Core® from greenTEG AG, and Tucky from E-TakesCare (Ajčević et al., 2022; Tamura et al., 2018). While these systems offer continuous measurements without cables, they suffer from key limitations. First, many exist only as single-use disposables, with associated cost barriers that prevent their use in low-income settings. Second, all existing options are too rigid and/or too large for neonates. Third, sensitivity to the environment including ambient temperature and/or humidity hinders accurate temperature measurements. Fourth, none offers the ability for multi-site on the body surface, time-synchronized operation.

In this work, we introduce an advanced, wireless temperature sensor characterized by miniaturized dimensions and a soft, skin-compatible encapsulation structure. Optimized designs enable continuous monitoring in the most challenging care environments (e.g. the neonatal intensive care unit), conformable placement in specific anatomical locations such as the floor of the axilla where the axillary artery is most superficial to the skin for enhanced accuracy, and targeted application to areas of localized skin inflammation or infection. Additional engineering strategies and material selections enable accurate sensing even in highly variable ambient temperature conditions including those associated with direct radiant warming and high humidity. The devices can deploy at multiple sites across the body, wirelessly networked for time-synchronized operation to a single mobile device. The result enables continuous, full-body measurements of temperature distributions. Resulting differentials between central and peripheral skin temperature, obtained without the burden of additional cables or excessive medical adhesives on fragile skin, are particularly valuable in tracking for early signs of sepsis in neonates (Bhandari, 2014; Gilfillan and Bhandari, 2017; Leante-Castellanos et al., 2012). As an additional set of features, this system simultaneously records other relevant physiological parameters (e.g. heart rate, respiratory rate, body position, vocalizations, and movement) via mechano-acoustic measurements of body motions and sounds captured using a high-bandwidth accelerometer. The following sections present (i) device configurations and applicable systems, (ii) rigorous evaluations of performance metrics in temperature sensing, (iii) time-synchronized operation of multiple sensor systems for spatiotemporal temperature mapping, (iv) estimations of core body temperature via axillary measurements, (v) demonstrations of tracking of additional vital signs and related information on patient status, and (iv) examples of the use on newborn babies in neonatal and pediatric intensive care units.

2. Methods

2.1. Encapsulating the electronics in a soft enclosure

A milling machine (MDX 540, Roland) produced customized aluminum molds with concave shapes to define top encapsulating layers in a medical grade, skin-compatible silicone elastomer (Silbione RTV-4420, Elkem) with white and blue pigments (Silicone Pigment, Smooth-On, 9:1) using a hot press machine (Auto Series Press, Carver) at 115 °C and 3000 lbs for 2 min. The bottom layers had thicknesses of 120 μm, separately prepared by spin-coating a silicone elastomer on an acrylic plate at 500 rpm for 1 min and curing at 70 °C in an oven for 20 min. Six layers of an insulating film (RTAZS, 0.2 mm, 0.038 W/mK, Blueshift) with a square-shaped hole was mounted onto the bottom encapsulating layer in a manner that covered the skin-facing NTC thermistor to form an air cavity ($3 \times 3 \times 1.2$ mm^3). Filling the top encapsulating layer in the mold with a silicone elastomer (Ecoflex 0030, Smooth-On) and then placing the electronics on the bottom layer completed the process by clamping the entire assembly and curing at 60 °C in an oven for 40 min. After cooling to room temperature, the encapsulated device was removed from the mold and the excess outline was cut away using a CO_2 laser (VLS3.60DT, Universal Laser Systems).

2.2. Circuit-level operation of the device

Fig. S1 shows the circuit-level aspects of device operation. In the main sensor unit, two LDOs (TPS7A02, Texas Instruments) convert the transferred power to a constant voltage of 1.8 V. One of the two LDOs remains active to enable Bluetooth communication; the other activates only when collecting data, to minimize standby power consumption (Fig. S2). The BLE SoC (ISP 1807, Insight SIP) controls these LDOs and provides power to the sensors through Analog-to-Digital Converting (ADC) pins with 16-bit resolution and digital General-Purpose Input/Output (GPIO) pins. Voltage divider circuits that include the NTC thermistors (10 kΩ, 3380 K, Murata Electronics) and reference resistors (10 kΩ, 0.1%, Vishay Dale) support robust capabilities in temperature sensing (Fig. S3). The IMU (BMI160, Bosch) can effectively capture not only changes in body orientation but also high frequency signals originating from cardiac cycles, respirations, and vocalizations such as crying. The resonance frequency of the Rx coil was set to the NFC standard (13.56 MHz) by adjusting capacitors connected in parallel. The rectifier (BAS4002, Infineon Tech.) converts the transferred AC voltage into a DC voltage, with a voltage regulator (LP2985, Texas Instruments) that maintains the output at 3.2 V. A pair of supercapacitors act as a charge reservoir to ensure stable operation during periods of low power transfer. A comparator (MIC842, Microchip Tech.) activates the LDO when the supercapacitors have sufficient charge to operate the main sensor unit.

2.3. 3D finite element analysis (FEA) modeling

The commercial software COMSOL Multiphysics enabled finite element analysis (FEA) modeling of heat transfer mechanisms through the device from the skin to the ambient. The three-dimensional (3D) FEA model simulated the device resting on the top surface of a 10-mm thick slab of PDMS as a skin phantom. The COMSOL interface used a 3D CAD file of the device layout with different material parts. The COMSOL simulation applied Fourier's law to model heat conduction in the device mathematically. The differential form of the heat equation is $q = -k\nabla T$, where q is the local heat flux density, k is the material's thermal conductivity, and ∇T is the temperature gradient. With the assumptions of constant pressure, negligible device deformation and no fluid movement in the device, the energy conservation was modeled in terms of temperature by the following differential equation: $\rho C_P \frac{\partial T}{\partial t} = \nabla \bullet (k\nabla T) + Q$, where ρ is the material's density, C_P is the specific heat capacity, and Q is the volumetric heat source. The left term reaches zero when the model reaches steady state, and $Q = 0$ indicates that the device does not generate heat. Thermal convection of air at a temperature of T_{air} defined heat transfer at the outer surfaces of the device with a heat transfer coefficient $h_{convection}$. The bottom surface of the phantom had a fixed temperature of 37 °C to simulate the core-body temperature. Heat transfer from the phantom to the device and the ambient air caused a temperature gradient sensed by two probes (NTC1 and NTC2) at different locations. The FEA model evaluated different configurations of the devices and analyzed the effects of T_{air} and $h_{convection}$ by parametric sweeps. The temperature gradients between NTC1 and NTC2 simulated

from different configurations helped to optimize the device design for enhanced temperature gradient and accurate skin temperature measurements. The results of temperature gradients and thermal profiles are summarized in Fig. S4. Various models with mesh densities ranging from 60 elements per cubic millimeter to 83 elements per cubic millimeter were analyzed to check the mesh independence and computational convergence, to a temperature difference less than 0.1 °C. The following parameters were used in the computations: thermal conductivity of 0.3 W/mK for the tissue; 0.21 W/mK for the electronics; 0.21 W/mK for the NTC thermistors; 0.038 W/mK for the insulating films; 0.2 W/mK for Ecoflex 00–30; 0.15 W/mK for Silbione 4420.

2.4. Measuring temperatures and body motions

A double-sided medical-grade silicone adhesive (2477 P, 3 M) secured the device on the skin. The temperature data were collected using a voltage divider circuit made of the series connection of the NTC thermistor (10 kΩ, 3380 K, Murata Electronics) and a reference resistor (10 kΩ, 0.1%, Vishay Dale). Motion data were captured using an IMU (BMI 160, Bosch) with 16-bit resolution, 0.061-mg sensitivity, 1600-Hz sampling rate, and ± 2 g acceleration range (adjustable up to ±16 g).

2.5. Procedure for monitoring the eczema patient

Wiping the skin with a 70% isopropyl alcohol pad (Alcohol Prep Pads, TopCare) removed oils and residue prior to measurements. Data collection occurred for 15 min from eight devices after waiting for 15 min following mounting to ensure temperature stabilization. A process of removing the devices, applying the topical steroid cream and waiting for 1 h preceded additional measurements following these same

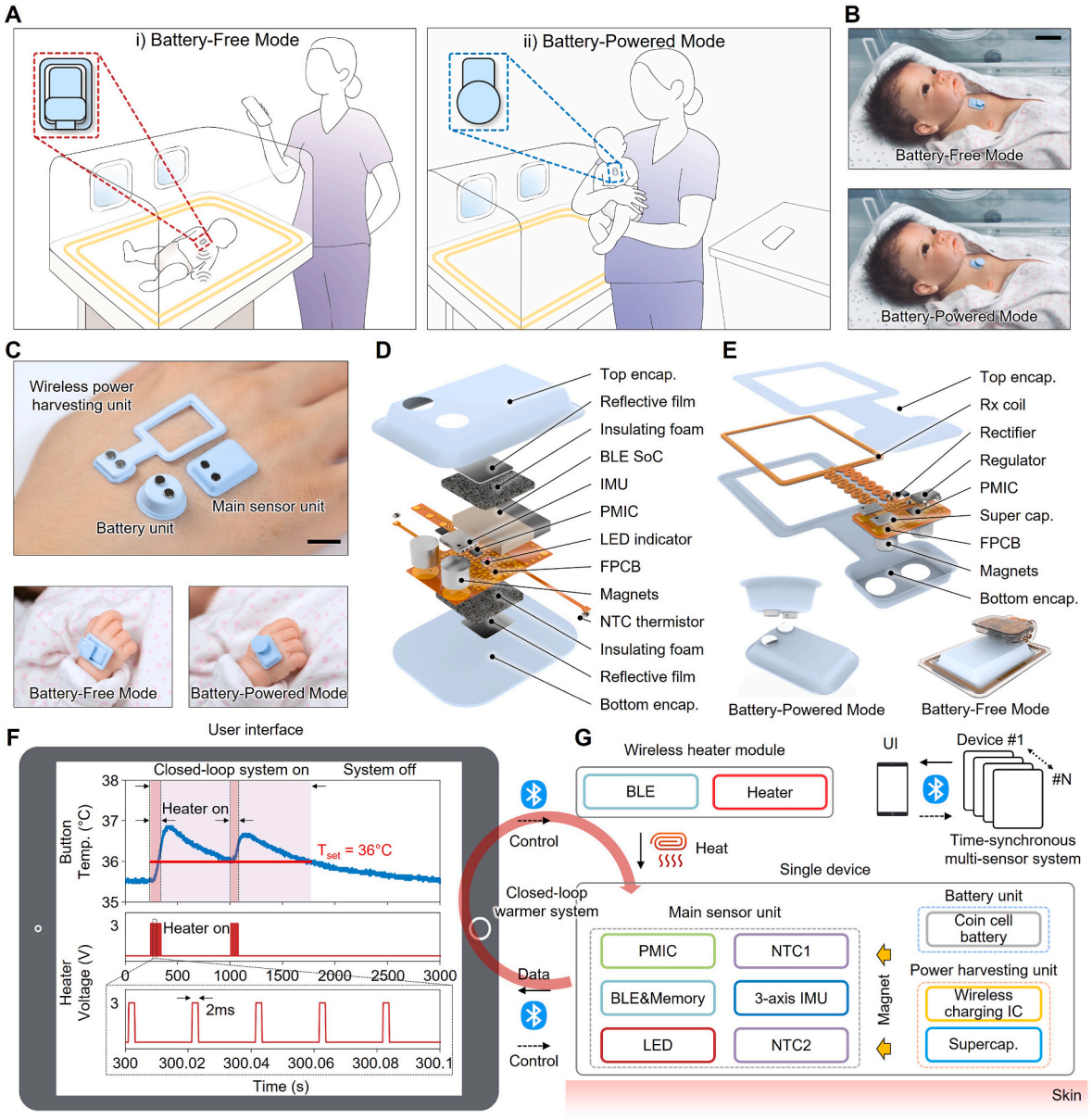

Fig. 1. (A) Schematic illustrations of modes for continuous vital signal monitoring using a 'button' device with different modes of power supply. (B) Photographs of devices on a realistic neonate model. The upper and bottom panels show the battery-free and battery-powered versions, respectively. (C) Photographs of three subsystems; the sensor, wireless power harvesting unit, and battery unit. (D)–(E) Exploded view schematic illustrations of these three units. (F)–(G) Experimental data and functional block diagram of a closed-loop warmer system for temperature regulation in an incubator. The system includes a button device, a customized user interface, and a wireless module for heating the local environment of the incubator. Multiple devices wirelessly connect to a single user interface (UI), as a time-synchronized multi-sensor system.

procedures.

2.6. Protocols for human subject studies

The studies were approved by the Northwestern University Institutional Review Board, Chicago, IL, USA (STU00202449 and STU00212522) and were registered on ClinicalTrials.gov (NCT02865070 and NCT04393558). All study-related procedures were carried out in accordance with the standards listed in the Declaration of Helsinki (1964) (World Medical, Association, 1964). For all subjects in neonatal and pediatric care units, a double-sided medical silicone adhesive (3 M, 2477 P) secured the device to the skin at the axillary and suprasternal notch for a few hours. Clinical staff assisted in placing the device. After each measurement session, the device was sterilized using 70% isopropyl alcohol, repeated twice.

3. Results

3.1. Device architecture, use cases and options in power sources

Fig. 1A presents illustrations of use cases that range from care in neonatal intensive-care units (NICUs) in hospitals to cribs in home settings. The system consists of a miniaturized wireless biosensor, referred to in the following as a button due to its small size and circular shape to maximize ease of use and anatomical placement, with options in both battery-free and battery-powered modes of operation. The latter relies on magnetic inductive coupling (Near-Field Communication, NFC, standards) for wireless power transfer from an external transmitting coil to a receiving coil built into the structure of the device. This design minimizes the size and weight of the system, with an operating range (tens of centimeters) that can support coverage throughout a standard incubator or crib. Replacing the antenna with a small battery eliminates the need for proximity to a transmission coil (Fig. S5). Both configurations use Bluetooth protocols for two-way wireless data communication, over distances of tens of meters. Fig. 1B and C displays photographs of such devices on a realistic doll and on the hand of an adult. The small sizes, versatile designs, and optimized thermal sensing capabilities of these devices represent important distinguishing characteristics over previously reported technologies of this general type.

Fig. 1D and E shows exploded-view illustrations of the main sensor and the wireless power harvesting sub-system, respectively. The former consists of a Power Management Integrated Circuit (PMIC), a Bluetooth Low Energy (BLE) System-on-Chip (SoC), temperature/motion sensor units, an LED indicator, and magnets, all mounted on a flexible printed circuit board (fPCB) using Surface-Mounted Technology (SMT). An emphasis here is on accurate measurements of temperature, with adequate time response. To this end, a commercial insulating foam and reflective film cover the body of the device to minimize the influence of the ambient on measurements of the temperature of the skin. Two Negative Temperature Coefficient (NTC) thermistors fold in a manner that orients one toward the skin and the other toward the ambient. A molded medical-grade silicone elastomer serves as a soft encapsulating structure. In the wireless power harvesting unit, the power receiving (Rx) coil connects through flexible copper traces to a rectifier, a voltage regulator, supercapacitors, a PMIC, and magnets for mechanically coupled interconnects.

The output of the PMIC supports skin- and ambient-facing temperature measurements and mechano-acoustic data collection using two NTC thermistors and a 3-axis Inertial Measurement Unit (IMU), respectively. These data pass to an embedded flash memory on the BLE SoC and then wirelessly transmit to a user interface on a BLE-enabled device such as a smartphone. An LED indicator serves as a visual alarm that can be activated based on the measured data and various, user-defined threshold settings. These data can also be transferred to external life support systems for automated control. An example involves active regulation of the temperature of a neonatal incubator according to the body temperature. Fig. 1F and **G** shows a closed-loop system that includes a button device, a customized user interface, and a wireless module for heating the local environment of the incubator. Regulation of the temperature follows from comparisons of the temperature of the baby to a desired body temperature ($T_{set} = 36\ ^{\circ}C$, here). Multiple devices can be located at different regions of the body, for time-synchronized operation. The data can also be uploaded to a secure Cloud platform for remote monitoring and analysis.

3.2. Performance benchmarking for temperature sensing

Fig. 2A shows a simplified schematic diagram of the battery-powered embodiment. In this sensor, a voltage divider circuit that includes an NTC thermistor (thermal sensor) and a reference resistor supports robust and stable temperature sensing capabilities. The sensing performance depends on the change in the temperature of the NTC itself, as influenced by three main factors: i) the external ambient environment, ii) the thermal mass of the NTC thermistor and the surrounding materials, and iii) the thermal contact between the NTC and the target. Six layers of a thermal insulating film (RTAZS, 0.2 mm, 0.038 W/mK, Blueshift) that cover the NTC on the side opposite to the skin minimize the influence of the external environmental on the measurements. This insulation increases, however, the thermal mass of the sensor and therefore increases the thermal response time. An air cavity ($3 \times 3 \times 1.2\ mm^3$) structure compensates for this effect by thermally isolating the NTC thermistor from the other body parts of the sensor. From a heat transfer perspective, reductions in the thickness of the encapsulating material between the NTC thermistor and the target improve the efficiency of heat transfer. Thus, the bottom encapsulating layer is selected to be thin ($<120\ \mu m$). A silicone elastomer (Ecoflex 00–30, 0.15 W/mK, Smooth-On) fills the other areas of the device. A molded elastomer with a different chemical formulation forms an encapsulating structure for the entire system (Silbione RTV-4420, 0.15 W/mK).

Fig. 2B and **C** presents finite element analysis (FEA) results for the temperature distribution inside the device, including locations of the skin- and ambient-facing NTC thermistors, with a thermally insulating air cavity structure (cavity) and without this cavity (control). For an ambient temperature of 18 °C, the skin-facing and ambient-facing regions of the former design are 0.1 °C higher and 0.65 °C lower, respectively, than the corresponding temperatures of the latter (left panel). Moreover, in all ambient temperature cases, the difference between skin and ambient temperatures obtained from the sensor with the cavity structure is greater than that of the control sensor (right panel). These results indicate that the cavity structure prevents heat from escaping and improves thermal isolation.

Detailed comparisons of capabilities for measurements of temperature involve clinical standard, hard-wired sensors (DeRoyal) designed for use in the NICU. Quantitative assessments focus on the accuracy, cyclic stability, humidity response, endurance and response time. Fig. 2D and **E** displays the results of tests that involve suspending these two types of devices in the air in an environmental chamber (LH-1.5, Associated Environmental Systems) (Fig. S6) with set temperatures from 30 to 45 °C maintained for 30 min each, at a relative humidity (RH) of 5%, based on guidance from the Food and Drug Administration (FDA). The data show excellent agreement (Fig. 2D). Fig. 2E displays the average temperature values and differences for 10 s (0.5 samples per sec, 20 data points) after the 30 min hold times. The differences in region 3 ($37\ ^{\circ}C < \text{Temperature} < 39\ ^{\circ}C$) are $\pm 0.1\ ^{\circ}C$, consistent with FDA requirements (Fig. S7). The standard deviations at 25 °C and 45 °C during cycle tests for the button device are 0.03 °C and 0.07 °C, respectively (Fig. 2F). Tests of sensitivity to humidity involve a set temperature of 36.5 °C for RH between 25.2 and 80.3% (Fig. 2G). Temperature fluctuations occur immediately after changing the RH for both sensors (the upper panel), but without any significant systematic dependence on RH (the lower panel), consistent with requirements for clinical use in an incubator. Fig. 2H shows the results of tests of the effects of storage of

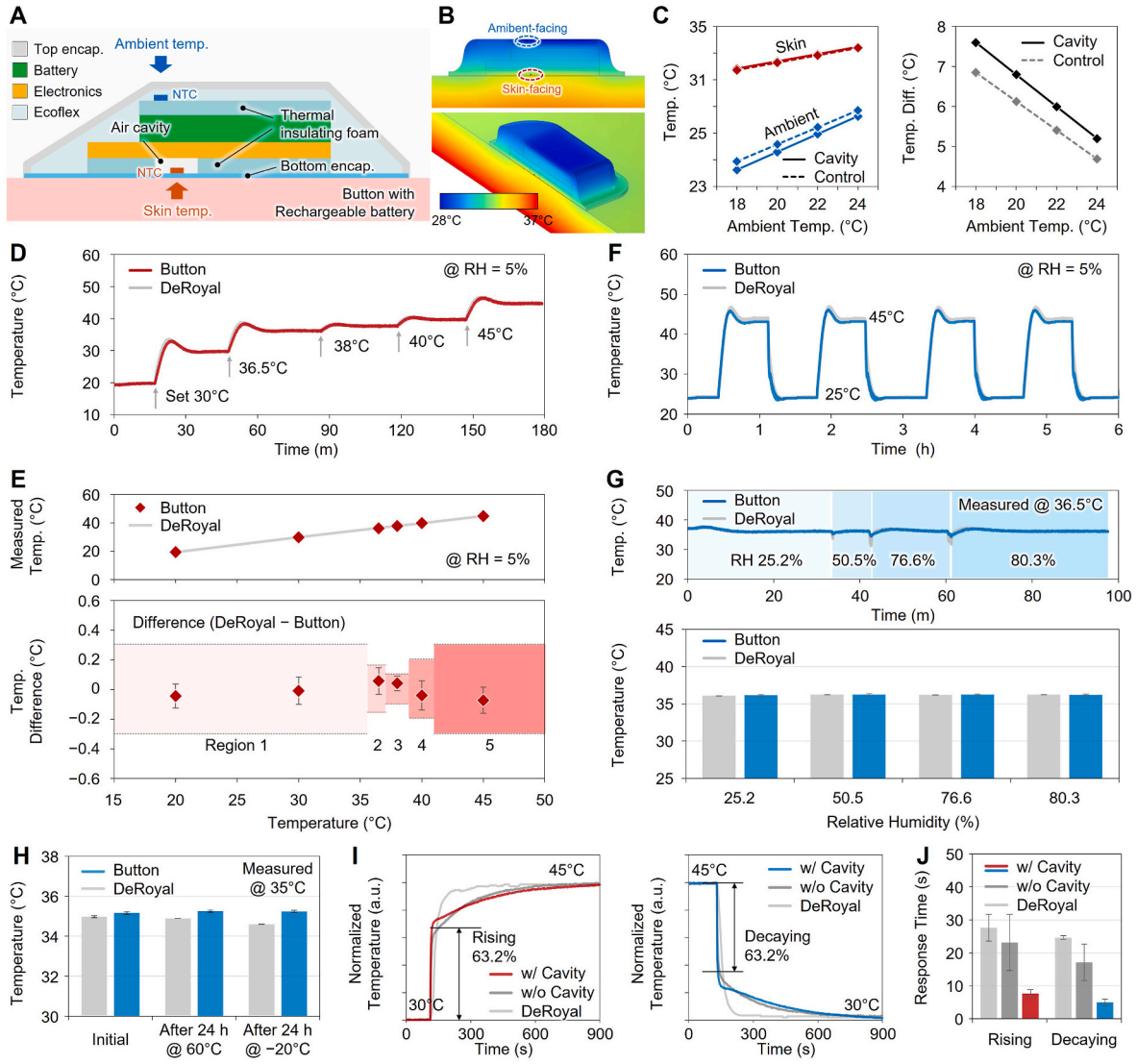

Fig. 2. (A) Schematic illustration of the device. The skin and ambient temperature can be monitored by the skin- and ambient-facing NTCs, respectively. (B) 3D FEA results for the distribution of temperature across a device without any thermal insulation (control). (C) 3D FEA results for the distribution of temperature across a device with thermally insulating air cavity structure. (D)–(E) Comparison of the accuracy of temperatures measured with a button device and a clinical-grade, hard-wired sensor (DeRoyal), for temperatures from 30 to 45 °C, with a residence time of 30 min at each setting. (F) Continuous temperature monitoring with the button and DeRoyal devices for temperature cycling from 25 to 45 °C and then 45 to 25 °C, for four iterations. (G) Tests of sensitivity to humidity for these two devices. The bottom panel shows the results after temperature saturation. (H) Tests of endurance, involving measurements at 35 °C after storage for 24-h in an oven at 60 °C, followed by a repeat of this measurement after 24 h storage at −20 °C. (I)–(J) Measurements of response time, involving rise and decay times (63.2% transition from an initial to a final temperature) following rapid changes in temperature.

the devices at high (60 °C) and low (−20 °C) temperatures, as an additional practical requirement. For a set temperature of 35 °C, the percent error after storage at 60 °C and −20 °C for 24 h is 0.3% and 0.2%, respectively. Fig. S8 also displays that the temperatures obtained from the skin- and ambient-facing NTC thermistors show good agreement according to the restricted temperature environment in the chamber, which indicates that both NTCs follow the external temperature. Fig. 2I and **J** displays the times to respond to abrupt changes in temperature for devices mounted first on a skin phantom placed on a hot plate at a temperature of 30 °C and then on another at 45 °C (Fig. S9). The response time refers to the time for the temperature to change from the initial value to 63.2% of the total change. For the button device with the cavity structure, rising and decaying times are 7.6 s and 5 s, respectively. The results of additional benchmarking studies with commercial sensors and those reported in the published literature appear in Tables S1 and S2, respectively.

3.3. Monitoring of local skin temperature

Fig. 3A shows data from a study that involves measuring the skin temperature from a healthy adult subject during a 5-h period of work and a 10-h period of sleep using a button device and a commercial wireless skin temperature sensor (Core, greenTEG AG) attached side-by-side on the lower chest. Bland–Altman (BA) plots show that the mean differences of the temperatures measured by these two devices are only 0.02 °C, and the upper and lower limits of the 95% confidence intervals (+1.96 SD and −1.96 SD) are 0.46 °C and −0.42 °C, respectively (Fig. 3B). Similar levels of the agreement appear in data collected continuously over a period of three days (Fig. 3C) from the chest area, except for times during device removal for showering. The button device offers advantages due to its small size, where the volume and weight are 11.8 and 3.9% of the average values of other wireless sensors, respectively. For example, mounting can occur on a wide range of anatomical locations of neonates including the chest, arms, legs, and even the axilla

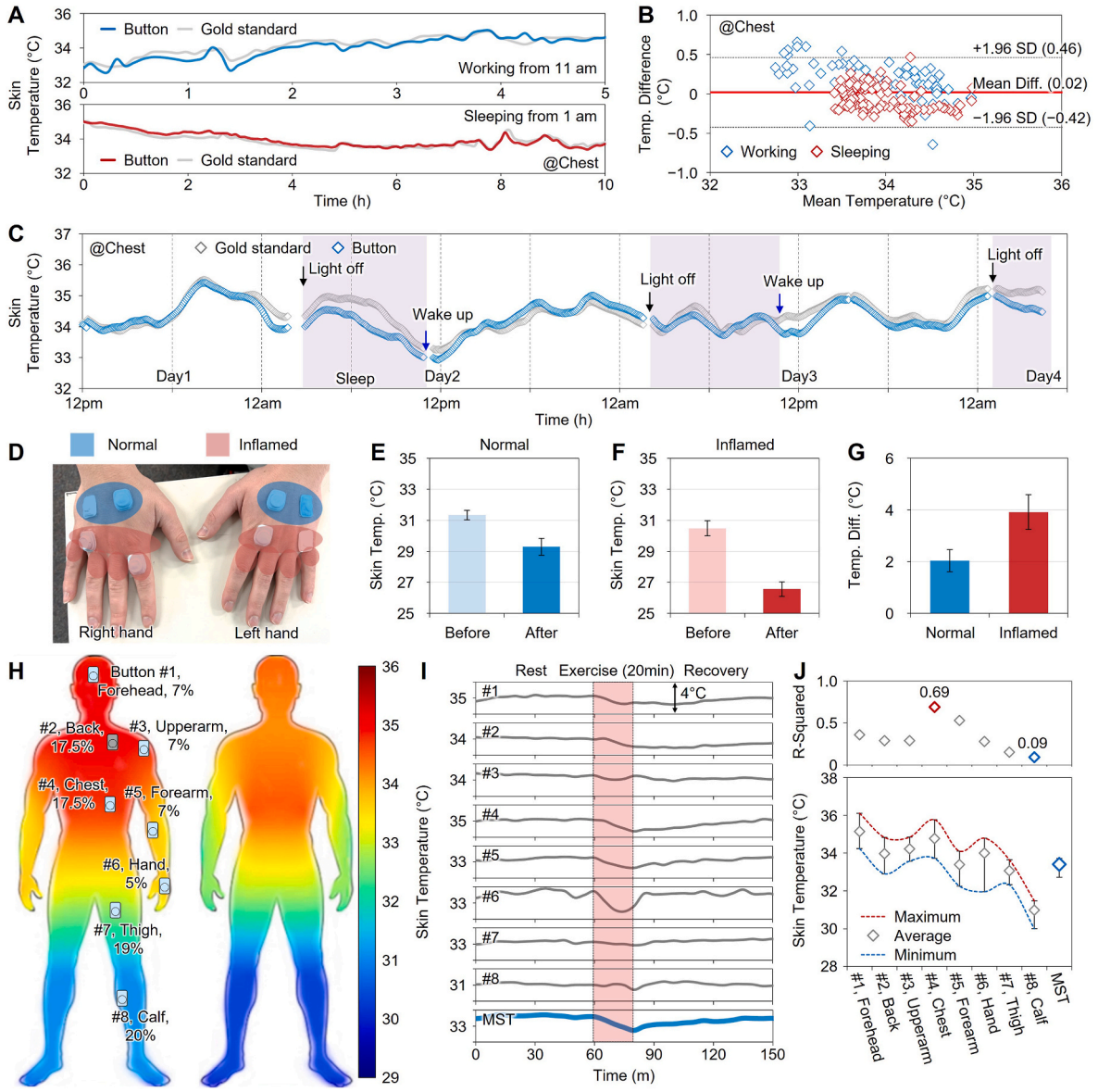

Fig. 3. (A) Skin temperature at the chest collected using a button device and a commercial wireless device (Core) during exercising and sleeping. (B) Corresponding Bland–Altman plots. (C) Circadian rhythms appear in temperatures measured across a period of three days. (D) Example of multi-device operation through the use of eight sensors mounted on the hands of an atopic dermatitis patient for recording changes in skin temperature before and after applying a topical steroid cream. (E)–(F) Average skin temperature of normal and inflamed regions of the skin before and after the steroid application. (G) Temperature difference between normal and inflamed skin after steroid application. (H) Results for mapping of skin temperature at eight different mounting locations (#1–8) using a wirelessly time-synchronized collection of devices and weight factors of corresponding body parts (%) before (left) and after (right) a 20-min exercise. (I) Continuous measurements of skin temperature at these locations and mean skin temperature (T_{MST}) calculated via a weighted sum of the local temperature. (J) Similarity factor (R-squared, R^2) between T_{MST} and temperatures of each location (upper panel). The temperature variations for the eight locations and T_{MST} during a workout test (lower panel).

(Fig. S10).

Wirelessly time-synchronized collections of these devices enable mapping of skin temperature across regions of interest, with good spatial resolution due to their miniaturized sizes (Fig. S11). Fig. 3D shows an example using eight devices mounted on the hands of an atopic dermatitis patient before and after applying a medium potency topical steroid cream (Triamcinolone Acetonide Cream USP, 0.1%, Perrigo). The target areas are the back of the hand (normal skin, blue color) and the base of the finger (inflamed skin by eczema, red color). Fig. 3E and **F** presents the average skin temperature of the normal and inflamed regions of the skin before and after steroid application, respectively. The temperature of normal and inflamed skin decreases from 31.3 to 29.3 °C and from 30.5 to 26.6 °C, respectively (Fig. 3G). Several potential clinical applications of this capability can be considered. First, the measurements may serve as a marker of inflammation (e.g. atopic dermatitis) or infection (e.g. superficial skin infections) not readily apparent by visual inspection. Because the main mechanism of topical steroids is vasoconstriction of peripheral skin vasculature, associated changes in temperature offer a surrogate to assessments of potency typically performed with laboratory calibrated chromameter to assess skin blanching.

As another application example, Fig. 3H shows changes before (left) and after (right) a 20-min exercise across eight representative body locations (forehead, back, upperarm, chest, forearm, hand, thigh, and calf from the top to bottom). The percentage value (P) corresponds to the ratio of the area of a local body part to the area of the entire body surface. Fig. 3I presents the results for each body region and the mean skin temperature (T_{MST}), defined as a weighted sum of the local skin

temperature (T_{Local}); $T_{MST} = \sum P \times T_{Local}$ over eight local body parts. The data indicate that T_{MST} decreases during exercise and recovers slowly afterward, consistent with expectations (Lan et al., 2019; Wu et al., 2020, 2023). Fig. 3J shows the similarity factor (R-squared, R^2) between T_{MST} and each local temperature (upper panel), along with variations in local skin temperatures and T_{MST} during exercise (lower panel). Here, the R^2 values for each location follow from a linear fitting model compared to T_{MST}. The R^2 of the chest and calf areas are the highest (0.69) and lowest (0.09), respectively. The average temperatures are highest at the forehead and lowest at the calf area. The maximum and minimum temperature changes occur at the hand and upper arm, respectively. The abilities for tracking both central and peripheral temperature have implications for occupational health and for wellness. For instance, hypothermia and hyperthermia are both life-threatening conditions that have significant biological variations. Thus, exposure risk depends on physical fitness, ambient conditions and clothing. In cold temperatures, frostbite, a major risk for military personnel, also applies to workers in outdoor occupations (e.g. construction workers) and to homeless individuals, with a cumulative lifetime incidence of 11%. Peripheral skin temperature is a key indicator of tissue injury. Miniaturized sensors such as these, when multiplexed and mounted on the extremities, may serve as an early warning system for high-risk individuals (Mäkinen et al., 2009; Min et al., 2021).

Fig. S12 displays similar skin temperature data recorded from subjects during sleep and exposure to a sauna (Fujimoto et al., 2021; Vargas et al., 2019). As expected, the T_{MST} during sleep is lower than that during exercise. The temperature on the back (#2) is relatively high, due likely due to contact with the bed. Compared to the sauna case, the temperatures in distal body parts including hands and calves are higher during sleep. In the sauna, the overall skin temperature increases shortly after exposure to an infrared heater and recovers slowly afterward. The highest temperature change occurs on the hand, likely because these

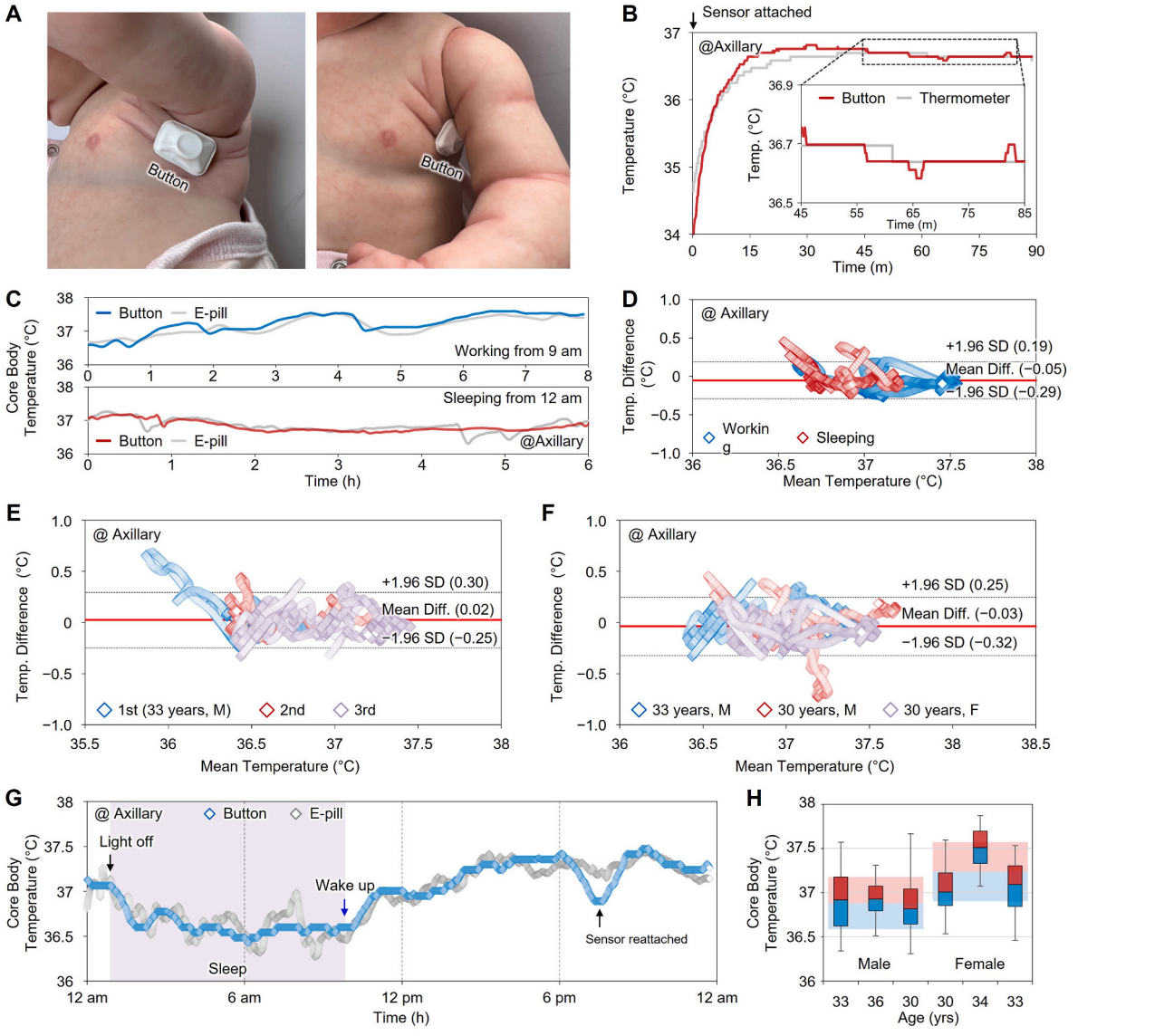

Fig. 4. (A) Photograph of a battery-powered device mounted under the arm of a realistic neonate model. (B) Skin temperature collected from a device and a digital thermometer at the axillary region of a healthy adult. The inset graph shows the temperature 45 min after mounting both sensors. (C) Core-body temperature estimated using a device mounted at the axillary region and using an ingestible sensor (E-pill) during exercising and sleeping. Here, the core-body temperature estimate corresponds to the addition of 1.2 °C to the axillary skin temperature ($T_{core} = T_{Button} + 1.2$ °C). (D) Corresponding Bland–Altman plot for these core-body temperatures. (E) Bland–Altman plot for core-body temperatures measured for 24 h from a healthy adult subject, repeated three times in sequence. (F) Bland–Altman plot for similar measurements from three healthy adults. (G) Circadian rhythms revealed by core-body temperatures measured at the axillary region for 24 h. (H) Variations in core-body temperature for 24 h from four health adult subjects.

distal parts of the body have enhanced sensitivity to the ambient temperature. Tracking changes in temperature during sleep-wake cycles may reveal disruptions in circadian rhythms, or signs of sleep related disorders (Boivin et al., 2022; Bracci et al., 2016; Lubov et al., 2021).

3.4. Monitoring of core body temperature

Core body temperature represents an essential parameter in defining health status, of particular importance for infants. Traditional measurements rely on sensors interfaced to oral, rectal or axillary locations (Sund-Levander et al., 2002; Taylor et al., 2014). Fig. 4A shows examples of a button device mounted under the arm of a realistic neonate model, enabled by the small device size. Fig. 4B compares data collected from an adult at this location, with simultaneous measurements captured using a digital thermometer (TC0521, PerfectPrime) at the same location. The miniaturized design allows the button device to be placed deep at the curvilinear pockets of the axilla, for improved core body temperature estimations compared to those based on existing systems. During the initial 15 min after attaching the sensors, both sets of data show sharp increases to steady state values of approximately 36.6 °C. Fig. 4C displays the temperature data from this region of a healthy adult subject along with results from an ingestible electronic pill (E-pill, e-Celsius, greenTEG), during working hours and sleeping. Here, a simple estimate of core body temperature that corresponds to the temperature of the skin plus 1.2 °C agrees well with data captured by the E-pill. Bland-Altman analysis indicates that the mean differences in temperature are only −0.05 °C, and the +1.96 SD/−1.96 SD are 0.19 °C/−0.29 °C, respectively (Fig. 4D). The BA plot in Fig. 4E shows that the mean differences of the core body temperature data collected from a healthy male adult three times in a row are only 0.02 °C, and the +1.96 SD/−1.96 SD are 0.3 °C/−0.25 °C, respectively. In addition, the mean differences collected from three healthy adult subjects are only −0.03 °C, and the +1.96 SD/−1.96 SD are 0.25 °C/−0.32 °C, respectively (Fig. 4F). Fig. S13 shows another core body temperature estimation technique using the dual temperature monitoring capability, following schemes reported in the previous work (Jeong et al., 2021). The core body temperature estimated via the 1-D heat transfer equation shows good agreement with oral temperature. 3D FEA results support the use of this 1-D approximation.

Core body temperature is also an excellent indicator of circadian rhythms (Refinetti, 2020; Refinetti and Menaker, 1992; Weinert, 2010). Fig. 4G presents variations over a 24-h period captured with these two devices. The results largely coincide even across this relatively narrow range of temperatures, approximately 1 °C. Fig. 4H presents similar data from six healthy adult subjects. The average temperatures of the female subjects studied here are 0.35 °C higher than those of males; the variations in temperature over a day are similar, approximately 1 °C (Hoffmann et al., 2012; Kim et al., 1998). Overall, the results indicate that the system meets all key accuracy and performance criteria of ISO 80601-2-56:2017, a consensus standard for clinical-grade thermometers.

3.5. Additional capabilities: heart rate, respiratory rate, and body orientation from neonates

As mentioned previously, the small size and weight of the devices make them well-suited for use with infants. Fig. 5A shows a photograph of a realistic neonate doll mounted with a device, a set of wired electrocardiogram (ECG) electrodes, and a wired temperature sensor (DeRoyal), to illustrate the burden of clinical standard monitoring equipment. The data from the button yield body orientations and motions, with vocalizations, respiratory sounds and cardiac amplitudes,

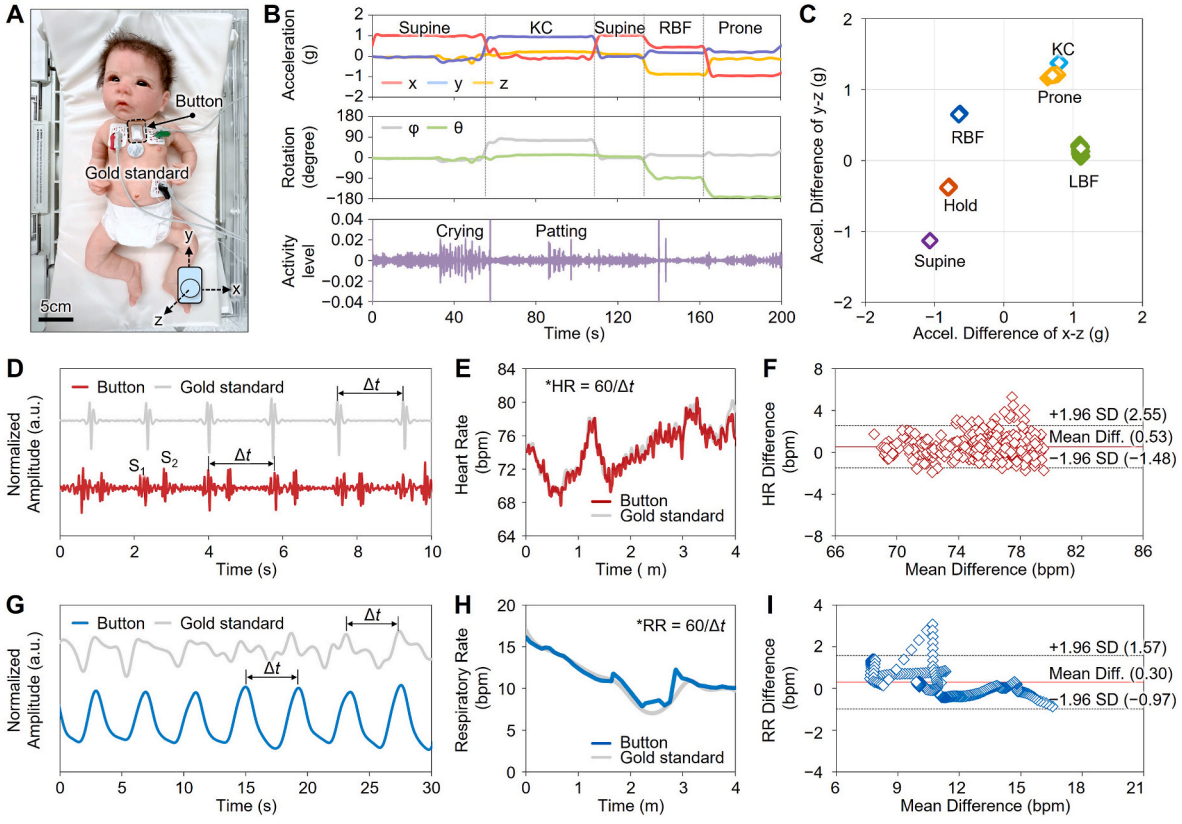

Fig. 5. (A) Photograph of a button device and hard-wired ECG and temperature sensors mounted on a realistic neonate doll. (B) Body orientation and activity data extracted from the 3-axis accelerometer. (C) Filtered acceleration data for various body positions. The x, y, and z-axis data were normalized and subtracted from each other. (D)–(F) Representative HR results from analysis of device data compared to those obtained with an ECG sensor. (G)–(I) Corresponding RR results.

along with heart rate, heart rate variability and respiratory rate. Fig. 5B shows three-axis acceleration data with respect to body orientations and activities. Here, the unit g represents the acceleration caused by gravity, and phi (φ) and theta (θ) denote the angle of the body from the supine position (supine) and the rotation angle of the central axis of the body, respectively. For the supine position, only the x-axis accelerates to approximately 1 g, and the other axes remain at 0. The kangaroo care (KC) scenario, where the mother holds the baby close to her chest while seated, leads to a y-axis acceleration of 1 g. The right body facing (RBF) position causes an acceleration of −1 g along the z-axis. The correlated rotation data show that the supine and prone positions have the same φ value of 0, but their θ values are different by −180°. In the case of the KC position, the φ value increases to approximately 90°, and the RBF position shows the θ value of −90°. The activity level data also include high-frequency features associated with crying and patting. These data agree with previously reported results (Chung et al., 2020; Lee et al., 2020). Fig. 5C and **S14** display extracted body orientation and rotation data for various situations. The distinguishable features in the acceleration and angle data enable clear classifications, important not only in tracking KC but also in setting alarms for dangerous positions that could lead to choking or impaired respiration.

Fig. 5D shows seismocardiography (SCG) and ECG data collected by the device and a clinical standard system (Dash 4000, GE), respectively. Post-processing the mechano-acoustic data using a bandpass filter from

Fig. 6. (A)–(B) Photographs of infants mounted with a device on a suprasternal notch (SN) for tracking of cardiopulmonary activity. (C) Photograph of an infant mounted with two devices on alternative locations for collecting global movements of the body. (D) Representative data obtained from a neonate (gestational age, GA: 39 weeks) in the NICU before, during, and after a blood draw. (E)–(F) Corresponding HR and RR changes for three healthy infant subjects. (G) Average HR and RR data for 11 infant subjects. (H) Skin temperature data in response to crying for a newborn baby (GA:42 weeks).

0.5 to 50 Hz facilitates extraction of the heart rate (HR) by dividing 60 by the time interval (Δt) between the S_1 peaks in the SCG signal (HR = $60/\Delta t$). Fig. 5E illustrates agreement between HR values from SCG and ECG. The BA plot indicates mean differences of 0.53 bpm, and the +1.96 SD/−1.96 SD are 2.55 bpm/−1.48 bpm, respectively (Fig. 5F). Respiration data follow from chest motions in the z-axis direction (normal to the surface of the skin). Post-processing in this case involves a lowpass filter with a cutoff of 0.5 Hz. Fig. 5G, **H**, and **5I** show the respiration rates collected from these data and the ECG waveforms. The BA plot shows that the mean difference of the RR data is only 0.30 bpm, and the +1.96 SD/−1.96 SD are 1.57 bpm/−0.97 bpm, respectively.

3.6. Representative data collected from patients in the NICU

Fig. 6A and **B** shows photographs of infants mounted with a device on a suprasternal notch (SN) for tracking of cardiopulmonary activity. Fig. 6C highlights alternative mounting locations, for collecting global movements of the body using two devices. Fig. 6D presents representative data from a neonate (gestational age, GA: 39 weeks) in the NICU before, during, and after a blood draw. The crying events recorded by the device during the procedure coincide with increases in HR and RR from 128 to 138 bpm and from 69 to 74 bpm, respectively. Fig. 6E and **F** shows similar changes in HR and RR for three healthy infant subjects. The graph in Fig. 6G corresponds to the average HR and RR data for 11 infant subjects, indicating increases of 8 and 3 bpm, respectively.

Fig. 6H displays an example that highlights the utility of temperature measurements. Newborns have underdeveloped function for thermoregulation. As a result, the body temperature of an infant can be strongly influenced by various factors, such as ambient temperature, health status, and even mental status (Bissinger and Annibale, 2010; Knobel and Holditch-Davis, 2007). The first graph shows normalized raw and envelop data of vocal activity (mostly crying) of a newborn baby (GA: 42 weeks) obtained through a cell phone (iPhone 14 Pro, Apple). The second graph shows the overall change in skin temperature measured from the chest area. The values decrease gradually from 36.3 to 36.2 °C, but with subtle variations that appear as increases in temperature. Applying a high-pass-filter (HPF) to these data highlights these changes. These features track with patterns of vocal activity, likely due to activation of the sympathetic nervous system during crying as a physical activity that also leads to coincidental vasodilation and increases in skin temperature. Furthermore, the amplitude of the crying correlates with the magnitude of the temperature change, as highlighted in the last graph. The combination of advanced thermal sensing capabilities with additional physiological monitoring might have important utility in the area of neonatal health.

4. Discussion and conclusion

This paper introduces a miniature wireless sensor with specific capabilities in advanced thermal monitoring, designed to operate continuously and reliably across a range of conditions and applications, including those related to the care of neonates in high ambient humidity environments with radiant heating such as those in incubators in the NICU. The key advances are in small, lightweight designs that can be deployed onto premature infants for homeostatic assessments, at specific locations for tracking inflammation or infection, and across optimized anatomical positions for accurate measurements of core body temperature. The device design strategies and material selections result in a sensor with excellent performance in temperature sensing in terms of accuracy (temperature difference <0.1 °C at region 3), insensitivity to humidity (without degradation at RH > 80%), and thermal response dynamics (rising and decaying time = 7.6 and 5 s, respectively). In the data obtained from healthy subjects, the measurement errors are in the range of 0.05 °C, exceeding regulatory requirements. Additional capabilities are in continuous monitoring of vital signals, especially for newborn babies and other vulnerable patient populations, in ways that are highly insensitive to ambient conditions. Time-synchronized operation across multiple body locations enables continuous, full-body measurements of spatio-temporal variations in temperature, including differentials between central and peripheral skin temperature for tracking of early signs of sepsis in neonates. Beyond thermal sensing, the ability of the sensor to measure other essential vital signs (e.g. respiratory rate and heart rate), physical activity levels, body orientation, and respiratory sounds provides further clinical value for a range of other applications from neonatal and infant care to sleep medicine and even pulmonary medicine.

Author Contributions

Seyong Oh: Experiment design, sensor fabrication, data acquisition, data analysis, Writing – original draft, Writing – review & editing. **Jae-Young Yoo:** Experiment design, sensor firmware development, user interface development, data acquisition, data analysis, Writing – review & editing. **Woo-Youl Maeng:** Experiment design, sensor fabrication, data acquisition, Writing – review & editing. **Seonggwang Yoo:** Experiment design, sensor fabrication. Writing – review & editing. **Tianyu Yang:** Heat transfer modeling simulation design. Writing – review & editing. **Susan M. Slattery:** Clinical test design, clinical data acquisition. Writing – review & editing. **Sara Pessano:** Clinical test design, clinical data acquisition. Writing – review & editing. **Emily Chung:** Sensor fabrication. Writing – review & editing. **Hyoyoung Jeong:** Experiment design. Writing – review & editing. **Jihye Kim:** Data acquisition. Writing – review & editing. **Hak-Young Ahn:** Data acquisition. Writing – review & editing. **Yeongdo Kim:** Data acquisition. Writing – review & editing. **Joohee Kim:** Data analysis. Writing – review & editing. **Shuai Xu:** Experiment design, data analysis. Writing – original draft, Writing – review & editing. **Debra E. Weese-Mayer:** Clinical test design, Writing – review & editing. **John A. Rogers:** Experiment design, Writing – original draft, Writing – review & editing.

Declaration of competing interest

The authors declare the following financial interests/personal relationships which may be considered as potential competing interests: Some of the authors are affiliated with a company, Sibel Health, that is pursuing commercialization of wireless devices for health monitoring, although not specifically the device reported in this manuscript.

Data availability

No data was used for the research described in the article.

Acknowledgements

The authors acknowledge funding from the Querrey-Simpson Institute for Bioelectronics and from grants from the National Research Foundation of Korea (NRF) grant funded by the Korea government (MSIT) (2021R1C1C2010180) and the DHA SBIR Phase II award (W81XWH22C0106).

Appendix A. Supplementary data

Supplementary data to this article can be found online at https://doi.org/10.1016/j.bios.2023.115545.

References

Ahrens, T., 2008. The most important vital signs are not being measured. Aust. Crit. Care 21 (1), 3–5.

Ajčević, M., Buoite Stella, A., Furlanis, G., Caruso, P., Naccarato, M., Accardo, A., Manganotti, P., 2022. A novel non-invasive thermometer for continuous core body temperature: comparison with tympanic temperature in an acute stroke clinical setting. Sensors 22 (13), 4760.

Amare, A., Kiros, D., Ramya, S., 2021. A Cost-Effective Digital Thermometer, Advances in Automation, Signal Processing, Instrumentation, and Control: Select Proceedings of I-CASIC 2020. Springer, pp. 2441–2446.
Areia, C., Biggs, C., Santos, M., Thurley, N., Gerry, S., Tarassenko, L., Watkinson, P., Vollam, S., 2021. The impact of wearable continuous vital sign monitoring on deterioration detection and clinical outcomes in hospitalised patients: a systematic review and meta-analysis. Crit. Care 25 (1), 351.
Bhandari, V., 2014. Effective biomarkers for diagnosis of neonatal sepsis. J. Pediatr. Infect.Dis. Soc. 3 (3), 234–245.
Bissinger, R.L., Annibale, D.J., 2010. Thermoregulation in very low-birth-weight infants during the golden hour: results and implications. Adv. Neonatal Care 10 (5), 230–238.
Boivin, D.B., Boudreau, P., Kosmadopoulos, A., 2022. Disturbance of the circadian system in shift work and its health impact. J. Biol. Rhythm. 37 (1), 3–28.
Bracci, M., Ciarapica, V., Copertaro, A., Barbaresi, M., Manzella, N., Tomasetti, M., Gaetani, S., Monaco, F., Amati, M., Valentino, M., Rapisarda, V., Santarelli, L., 2016. Peripheral skin temperature and circadian biological clock in shift nurses after a day off. Int. J. Mol. Sci. 17 (5), 623.
Cardona-Morrell, M., Prgomet, M., Lake, R., Nicholson, M., Harrison, R., Long, J., Westbrook, J., Braithwaite, J., Hillman, K., 2016. Vital signs monitoring and nurse–patient interaction: a qualitative observational study of hospital practice. Int. J. Nurs. Stud. 56, 9–16.
Castrodale, V., Rinehart, S., 2014. The golden hour: improving the stabilization of the very low birth-weight infant. Adv. Neonatal Care 14 (1), 9–14.
Chung, H.U., Rwei, A.Y., Hourlier-Fargette, A., Xu, S., Lee, K., Dunne, E.C., Xie, Z., Liu, C., Carlini, A., Kim, D.H., Ryu, D., Kulikova, E., Cao, J., Odland, I.C., Fields, K.B., Hopkins, B., Banks, A., Ogle, C., Grande, D., Park, J.B., Kim, J., Irie, M., Jang, H., Lee, J., Park, Y., Kim, J., Jo, H.H., Hahm, H., Avila, R., Xu, Y., Namkoong, M., Kwak, J.W., Suen, E., Paulus, M.A., Kim, R.J., Parsons, B.V., Human, K.A., Kim, S.S., Patel, M., Reuther, W., Kim, H.S., Lee, S.H., Leedle, J.D., Yun, Y., Rigali, S., Son, T., Jung, I., Arafa, H., Soundararajan, V.R., Ollech, A., Shukla, A., Bradley, A., Schau, M., Rand, C.M., Marsillio, L.E., Harris, Z.L., Huang, Y., Hamvas, A., Paller, A. S., Weese-Mayer, D.E., Lee, J.Y., Rogers, J.A., 2020. Skin-interfaced biosensors for advanced wireless physiological monitoring in neonatal and pediatric intensive-care units. Nat. Med. 26 (3), 418–429.
Crawford, D., Hicks, B., Thompson, M., 2006. Which thermometer? Factors influencing best choice for intermittent clinical temperature assessment. J. Med. Eng. Technol. 30 (4), 199–211.
Donnellan, D., Moore, Z., Patton, D., O'Connor, T., Nugent, L., 2020. The effect of thermoregulation quality improvement initiatives on the admission temperature of premature/very low birth-weight infants in neonatal intensive care units: a systematic review. J. Spec. Pediatr. Nurs. (JSPN) 25 (2), e12286.
Eddahchouri, Y., Peelen, R.V., Koeneman, M., Touw, H.R.W., van Goor, H., Bredie, S.J. H., 2022. Effect of continuous wireless vital sign monitoring on unplanned ICU admissions and rapid response team calls: a before-and-after study. Br. J. Anaesth. 128 (5), 857–863.
Elliott, M., Coventry, A., 2012. Critical care: the eight vital signs of patient monitoring. Br. J. Nurs. 21 (10), 621–625.
Fujimoto, T., Fujii, N., Dobashi, K., Cao, Y., Matsutake, R., Takayanagi, M., Kondo, N., Nishiyasu, T., 2021. Effects of low-intensity exercise on local skin and whole-body thermal sensation in hypothermic young males. Physiol. Behav. 240, 113531.
Gilfillan, M., Bhandari, V., 2017. Biomarkers for the diagnosis of neonatal sepsis and necrotizing enterocolitis: clinical practice guidelines. Early Hum. Dev. 105, 25–33.
Hoffmann, M.E., Rodriguez, S.M., Zeiss, D.M., Wachsberg, K.N., Kushner, R.F., Landsberg, L., Linsenmeier, R.A., 2012. 24-h core temperature in obese and lean men and women. Obesity 20 (8), 1585–1590.
Jeong, H., Lee, J.Y., Lee, K., Kang, Y.J., Kim, J.-T., Avila, R., Tzavelis, A., Kim, J., Ryu, H., Kwak, S.S., Kim, J.U., Banks, A., Jang, H., Chang, J.-K., Li, S., Mummidisetty, C.K., Park, Y., Nappi, S., Chun, K.S., Lee, Y.J., Kwon, K., Ni, X., Chung, H.U., Luan, H., Kim, J.-H., Wu, C., Xu, S., Banks, A., Jayaraman, A., Huang, Y., Rogers, J.A., 2021. Differential cardiopulmonary monitoring system for artifact-canceled physiological tracking of athletes, workers, and COVID-19 patients. Sci. Adv. 7 (20), eabg3092.
Kim, H., Richardson, C., Roberts, J., Gren, L., Lyon, J.L., 1998. Cold hands, warm heart. Lancet 351 (9114), 1492.
Knobel, R., Holditch-Davis, D., 2007. Thermoregulation and heat loss prevention after birth and during neonatal intensive-care unit stabilization of extremely low-birthweight infants. J. Obstet. Gynecol. Neonatal Nurs. 36 (3), 280–287.
Knobel, R.B., 2014. Thermal stability of the premature infant in neonatal intensive care. N.born Infant Nurs. Rev. 14 (2), 72–76.
Lan, L., Xia, L., Tang, J., Wyon, D.P., Liu, H., 2019. Mean skin temperature estimated from 3 measuring points can predict sleeping thermal sensation. Build. Environ. 162, 106292.
Leante-Castellanos, J.L., Lloreda-García, J.M., García-González, A., Llopis-Baño, C., Fuentes-Gutiérrez, C., Alonso-Gallego, J.Á., Martínez-Gimeno, A., 2012. Central-peripheral temperature gradient: an early diagnostic sign of late-onset neonatal sepsis in very low birth weight infants. J. Perinat. Med. 40 (5), 571–576.
Lee, K., Ni, X., Lee, J.Y., Arafa, H., Pe, D.J., Xu, S., Avila, R., Irie, M., Lee, J.H., Easterlin, R.L., 2020. Mechano-acoustic sensing of physiological processes and body motions via a soft wireless device placed at the suprasternal notch. Nat. Biomed. Eng. 4 (2), 148–158.
Lockwood, C., Conroy-Hiller, T., Page, T., 2004. Vital signs. JBI Libr. Syst. Rev. 2 (6), 1–38.
Lubov, J.E., Cvammen, W., Kemp, M.G., 2021. The impact of the circadian clock on skin physiology and cancer development. Int. J. Mol. Sci. 22 (11), 6112.
Mäkinen, T.M., Jokelainen, J., Näyhä, S., Laatikainen, T., Jousilahti, P., Hassi, J., 2009. Occurrence of frostbite in the general population – work-related and individual factors. Scand. J. Work. Environ. Health (5), 384–393.
Min, J.-y., Choi, Y.-S., Lee, H.-S., Lee, S., Min, K.-b., 2021. Increased cold injuries and the effect of body mass index in patients with peripheral vascular disease. BMC Publ. Health 21 (1), 294.
Refinetti, R., 2020. Circadian rhythmicity of body temperature and metabolism. Temperature 7 (4), 321–362.
Refinetti, R., Menaker, M., 1992. The circadian rhythm of body temperature. Physiol. Behav. 51 (3), 613–637.
Smith, J., Alcock, G., Usher, K., 2013. Temperature measurement in the preterm and term neonate: a review of the literature. Neonatal Netw. 32 (1), 16–25.
Sund-Levander, M., Forsberg, C., Wahren, L.K., 2002. Normal oral, rectal, tympanic and axillary body temperature in adult men and women: a systematic literature review. Scand. J. Caring Sci. 16 (2), 122–128.
Tamura, T., Huang, M., Togawa, T., 2018. Current developments in wearable thermometers. Adv. Biomed. Eng. 7, 88–99.
Taylor, N.A.S., Tipton, M.J., Kenny, G.P., 2014. Considerations for the measurement of core, skin and mean body temperatures. J. Therm. Biol. 46, 72–101.
Uslu, S., Ozdemir, H., Bulbul, A., Comert, S., Bolat, F., Can, E., Nuhoglu, A., 2011. A comparison of different methods of temperature measurements in sick newborns. J. Trop. Pediatr. 57 (6), 418–423.
Vargas, N.T., Chapman, C.L., Johnson, B.D., Gathercole, R., Schlader, Z.J., 2019. Exercise intensity independently modulates thermal behavior during exercise recovery but not during exercise. J. Appl. Physiol. 126 (4), 1150–1159.
Weenk, M., Koeneman, M., van de Belt, T.H., Engelen, L.J.L.P.G., van Goor, H., Bredie, S. J.H., 2019. Wireless and continuous monitoring of vital signs in patients at the general ward. Resuscitation 136, 47–53.
Weinert, D., 2010. Circadian temperature variation and ageing. Ageing Res. Rev. 9 (1), 51–60.
World Medical 1964., Association. Declaration of helsinki. http://www. med. or. jp/wma/helsinki02_j. html.
Wu, Y., Liu, H., Li, B., Jokisalo, J., Kosonen, R., Cheng, Y., Zhao, W., Yuan, X., 2020. Evaluation and modification of the weighting formulas for mean skin temperature of human body in winter conditions. Energy Build. 229, 110390.
Wu, Y., Zhang, Z., Liu, H., Cui, H., Cheng, Y., 2023. Optimal local skin temperatures for mean skin temperature estimation and thermal comfort prediction of seated person in thermally stratified environments. J. Therm. Biol. 111, 103389.
Xu, H., Li, P., Yang, Z., Liu, X., Wang, Z., Yan, W., He, M., Chu, W., She, Y., Li, Y., Cao, D., Yan, M., Zhang, Z., 2020. Construction and application of a medical-grade wireless monitoring system for physiological signals at general wards. J. Med. Syst. 44 (10), 182.
Xu, S., Kim, J., Walter, J.R., Ghaffari, R., Rogers, J.A., 2022. Translational gaps and opportunities for medical wearables in digital health. Sci. Transl. Med. 14 (666), eabn6036.